

Optical-resolution photoacoustic microscopy with a needle-shaped beam

Received: 8 June 2022

Accepted: 19 October 2022

Published online: 01 December 2022

 Check for updates

Rui Cao ^{1,7}, Jingjing Zhao^{2,7}, Lei Li¹, Lin Du ³, Yide Zhang ¹, Yilin Luo¹, Laiming Jiang⁴, Samuel Davis ¹, Qifa Zhou⁴, Adam de la Zerda^{2,5,6}  & Lihong V. Wang ¹ 

Optical-resolution photoacoustic microscopy can visualize wavelength-dependent optical absorption at the cellular level. However, this technique suffers from a limited depth of field due to the tight focus of the optical excitation beam, making it challenging to acquire high-resolution images of samples with uneven surfaces or high-quality volumetric images without *z* scanning. To overcome this limitation, we propose needle-shaped beam photoacoustic microscopy, which can extend the depth of field to around a 28-fold Rayleigh length via customized diffractive optical elements. These diffractive optical elements generate a needle-shaped beam with a well-maintained beam diameter, a uniform axial intensity distribution and negligible sidelobes. The advantage of using needle-shaped beam photoacoustic microscopy is demonstrated via both histology-like imaging of fresh slide-free organs using a 266 nm laser and *in vivo* mouse-brain vasculature imaging using a 532 nm laser. This approach provides new perspectives for slide-free intraoperative pathological imaging and *in vivo* organ-level imaging.

Over the past decades, rapid developments in optical imaging technologies have revolutionized life science. For high-resolution optical imaging, a tight optical focus is usually needed to achieve the diffraction-limited resolution in optical microscopy, resulting in a limited depth of field (DOF). This narrow DOF causes the degradation of lateral resolution at a distance away from the optical focal plane. It hinders the fast high-resolution imaging of slide-free specimens with irregular surfaces or three-dimensional (3D) volumetric imaging of organs, which usually requires time-consuming axial scanning at multiple planes as well as complicated image processing. For time-sensitive imaging applications like intraoperative histology or cerebral haemodynamics, the capability to directly image irregular surfaces with a large DOF at high resolution is desired. However, a large DOF with a tight optical focus for high-resolution imaging is not easily achievable.

To address the need for an extended DOF in high-resolution microscopes, researchers have explored different approaches. An extended DOF can be achieved via dynamic remote focusing or decoupled illumination and detection (for example, as in a light sheet microscope)^{1–6}. Nonetheless, this requires complicated geometry and increases the system complexity and cost. Alternatively, multi-plane microscopes have been implemented through spatial and spectral multiplexing techniques^{7–10}. However, 3D multi-plane imaging is susceptible to misalignment of the detection channels and demands accurate calibration of the image planes before imaging. Fourier ptychographic microscopy uses a simple configuration and adopts a wavefront correction strategy to extend the DOF computationally¹¹. However, the image-reconstruction algorithm for Fourier ptychographic microscopy uses a thin sample target transilluminated with oblique plane waves,

¹Caltech Optical Imaging Laboratory, Andrew and Peggy Cherg Department of Medical Engineering, Department of Electrical Engineering, California Institute of Technology, Pasadena, CA, USA. ²Department of Structural Biology, Stanford University School of Medicine, Stanford University, Stanford, CA, USA. ³Department of Electrical and Systems Engineering, University of Pennsylvania, Philadelphia, PA, USA. ⁴Department of Biomedical Engineering and Ophthalmology, Viterbi School of Engineering, University of Southern California, Los Angeles, CA, USA. ⁵Biophysics Program, Molecular Imaging Program, and Bio-X Program at Stanford University, Stanford, CA, USA. ⁶Chan Zuckerberg Biohub, San Francisco, CA, USA. ⁷These authors contributed equally: Rui Cao, Jingjing Zhao.  e-mail: adlz@stanford.edu; LWV@caltech.edu

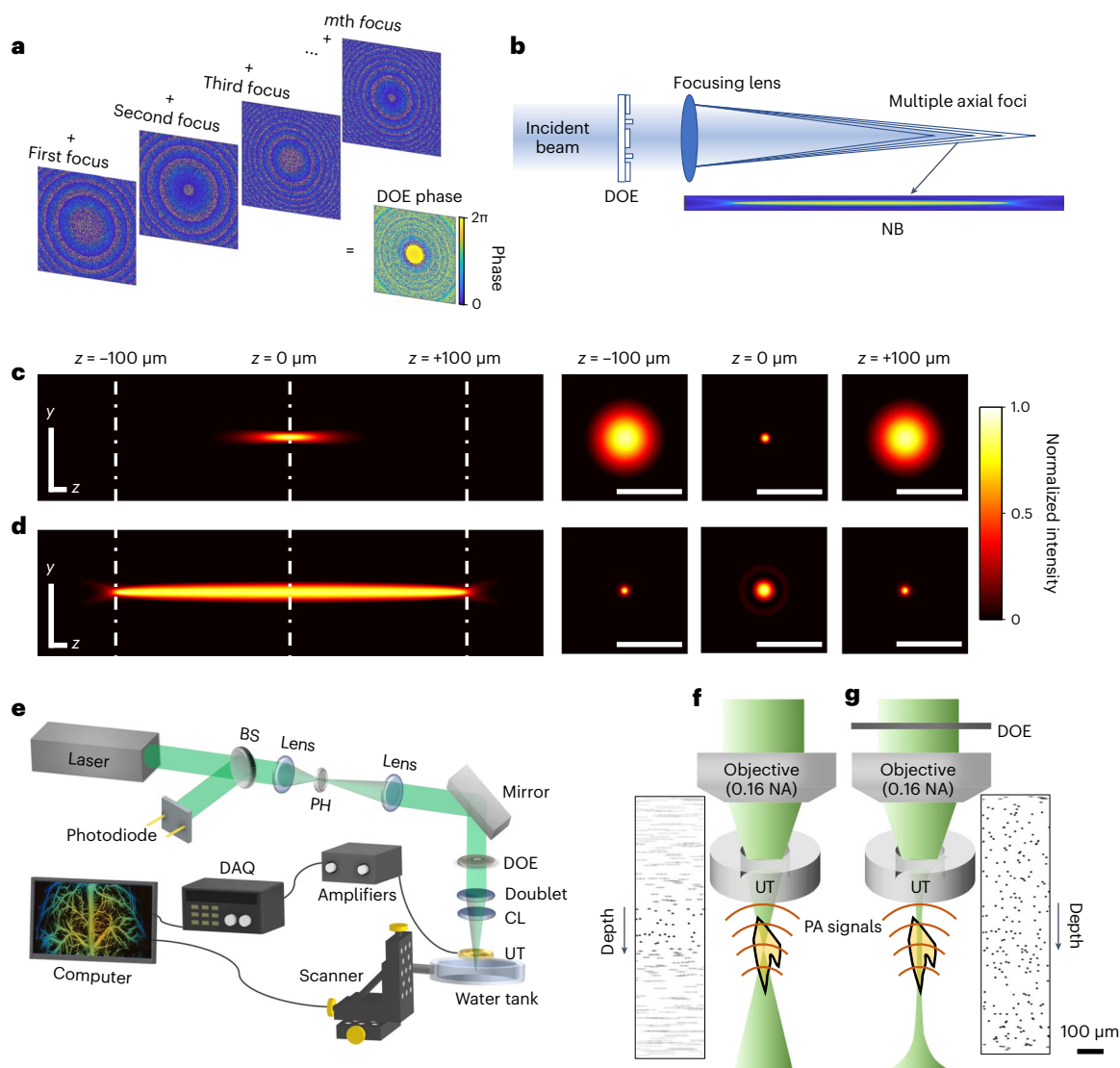


Fig. 1 | Principle of NB-PAM with a customized DOE. **a**, DOE phase pattern for an NB composed of multiple phases of M foci. **b**, Principle of a DOE combining M foci to form the desired NB. **c**, y - z profile of a Gaussian beam with a focal spot size of $1.2\ \mu\text{m}$ at $266\ \text{nm}$ (left) and x - y profiles (right) at different z positions. Scale bars, $10\ \mu\text{m}$. **d**, y - z profile of the NB generated by the DOE for the $200 \times 1.2\ \mu\text{m}$ NB at $266\ \text{nm}$ (left) and x - y profiles (right) at different z positions. Scale bars, $10\ \mu\text{m}$. The colour scale applies to both **c** and **d**. **e**, Experimental setup

of the NB-PAM system. BS, beam sampler; PH, pinhole; CL, correction lens; UT, ultrasonic transducer; DAQ, data acquisition. **f,g**, Principle of conventional GB-PAM (**f**) and NB-PAM (**g**). Simulated y - z projection images of uniformly distributed microspheres with a diameter of $7\ \mu\text{m}$ show the difference between GB-PAM with a $0.16\ \text{NA}$ (numerical aperture) and NB-PAM with a $0.16\ \text{NA}$ and the $1,000 \times 2.3\ \mu\text{m}$ DOE. Scale bar applies to both **f** and **g**.

limiting its applications for imaging thick specimens or organs in vivo. In addition, many researchers have applied non-diffracting beams (for example, a Bessel beam or an Airy beam) for extended DOFs in microscopy^{12–18}. However, the image quality usually suffers from severe sidelobes and low efficiency¹⁹. Recently, deep learning techniques have been applied to improve the DOF^{20–22}, although intensive training with lots of ground-truth data are needed, which may not be easy to acquire for specific subjects.

As an emerging technology, photoacoustic microscopy (PAM) can directly image the distribution of intrinsic or extrinsic optical absorbers by detecting optical-absorption-induced acoustic signals^{23,24}. Benefiting from the rich intrinsic contrasts in biological tissues, label-free PAM has been demonstrated in the imaging of various biological components, such as DNA/RNA^{25–27}, cytochromes²⁸, haemoglobin^{29–31}, melanomas³² and lipids^{33,34}. Different from other pure optical imaging techniques, 3D volumetric photoacoustic images can be directly

reconstructed with only two-dimensional (2D) scanning utilizing the time-of-flight information carried by the photoacoustic signals²³. For high-resolution imaging, optical-resolution photoacoustic microscopy (OR-PAM) with a tight optical focus has been implemented^{35,36}. However, OR-PAM still suffers from the trade-off between the DOF and the spatial resolution as other optical microscopy techniques—a higher spatial resolution corresponds to a narrower DOF, which compromises the image quality due to out-of-focus blurring in volumetric imaging or uneven surface imaging. Many efforts have been made in PAM to extend the DOF, such as utilizing Bessel beams^{37–39}, dynamic focusing^{40–42}, synthetic aperture focusing techniques^{43–45} and structured illumination^{46,47}, but these methods suffer from strong sidelobes, a slowdown of the imaging or complicated post-processing procedures.

To fill this gap, we present optical-resolution needle-shaped beam photoacoustic microscopy (NB-PAM) with an extended DOF via customized diffractive optical elements (DOEs). The needle-shaped beam

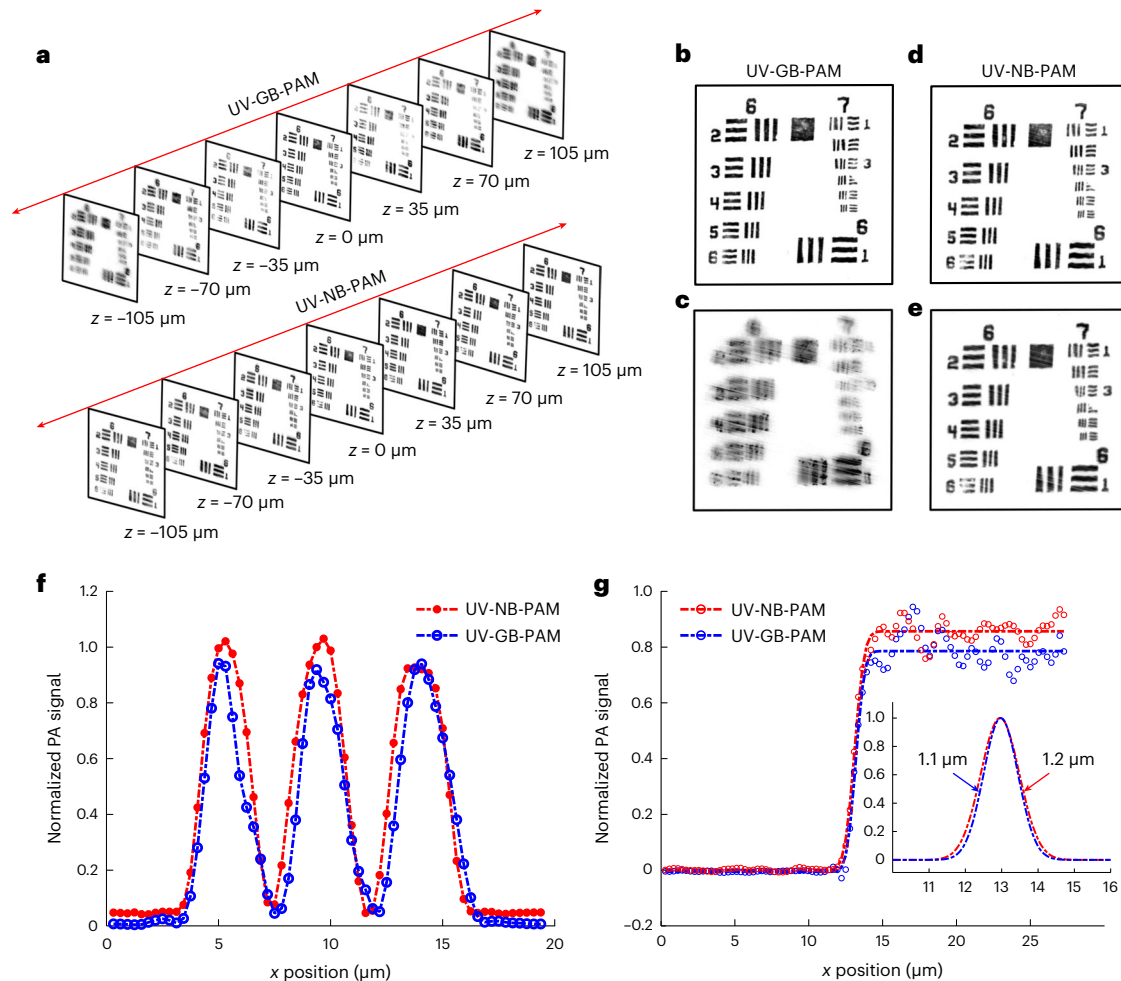


Fig. 2 | Characterization of UV-NB-PAM in comparison with that of conventional UV-GB-PAM. a, Images of a 1951 USAF resolution target at different axial positions acquired using UV-GB-PAM with a 0.16 NA (top) and UV-NB-PAM with the $200 \times 1.2 \mu\text{m}$ NB (bottom). The focal plane for UV-GB-PAM is at $z = 0 \mu\text{m}$. **b, c** Close-up images acquired using conventional UV-GB-PAM at $z = 0 \mu\text{m}$ (**b**) and $z = +105 \mu\text{m}$ (**c**). **d, e** Close-up images acquired using UV-NB-PAM

at $z = 0 \mu\text{m}$ (**d**) and $z = +105 \mu\text{m}$ (**e**). **f**, Profile of element 6 from group 7 measured using conventional UV-GB-PAM and UV-NB-PAM at $z = 0 \mu\text{m}$. **g**, Lateral FWHM resolution measured by imaging a sharp edge and quantified using edge spread functions and derived line spread functions (inset). The dashed lines in **f** and **g** indicate the measured profiles.

(NB) generated by the DOE is shown to have a DOF of up to a 28-fold Rayleigh length, while maintaining a relatively constant beam diameter, a uniform axial intensity distribution and negligible sidelobes. As a thin glass plate, the DOE can be easily integrated into an existing optical system without rebuilding the optical setup (for example, it can be placed in front of the objective lens). We demonstrate NB-PAM with an extended DOF for irregular surface imaging and volumetric imaging without z scanning. The histology-like photoacoustic imaging of fresh and slide-free organs was achieved using ultraviolet NB-PAM (UV-NB-PAM) at 266 nm, and in vivo mouse-brain vasculature images were acquired using visible NB-PAM (VIS-NB-PAM) at 532 nm.

Results

The principle of NB-PAM via DOEs

To form the NB, we developed DOEs to generate numerous closely adjacent foci along the axial direction (Fig. 1a, b). The beam length can be flexibly adjusted by increasing or decreasing the number of foci. The DOE phase is formulated as $P_{\text{DOE}}(x, y) = \sum_{m=1}^M \{ [-\pi n(x^2 + y^2)(1/f_m - 1/f) / \lambda - \pi mA] \text{Loc}_m(x, y) \}$, where (x, y) is the planar coordinate, λ is the light wavelength, f is the objective focal length in the medium, f_m is the chosen focal position, n is the refractive index of the surrounding medium, M is the foci

number, m is the focus index, $\text{Loc}_m(x, y)$ is a binary matrix to allocate the DOE pixels, A is a coefficient, πmA is the phase regulator responsible for adjusting the beam diameter, and the item $[-\pi n(x^2 + y^2)(1/f_m - 1/f) / \lambda - \pi mA]$ aims to shift the focus from f to f_m (Supplementary Fig. 1). The DOE pixels are equally and randomly allocated into m subsets (Fig. 1a), each of which belongs to one specific focus: for example, for the pixel (x, y) allocated to f_1 , $\text{Loc}_1(x, y) = 1$ and $\text{Loc}_{m \neq 1}(x, y) = 0$. The beam length is determined by $(f_m - f_1)$. The rule for determining the number of foci M is to control the average interval between two neighbouring foci with no more than one Rayleigh length. We set f_1 to be coincident with the objective lens focus f . Therefore, the NB can be generated using a customized DOE with the corresponding objective lens, as shown in Fig. 1b. The DOE was fabricated using a 500- μm -thick fused silica substrate (Supplementary Fig. 2a), which has rectangular pixels with an alignment error of around one micrometre via the four-times lithography to achieve 16 heights (Supplementary Fig. 2b). Further characterization details for the DOE fabrication can be found in Supplementary Fig. 2c–f and Supplementary Table 1.

We designed two DOEs, for UV-NB-PAM (266 nm) and VIS-NB-PAM (532 nm). The phase patterns for these two fabricated DOEs can be found in Supplementary Fig. 3a, b. The DOEs contain $1,024 \times 1,024$ pixels with a feature size of 10 or 15 μm , depending on the input beam

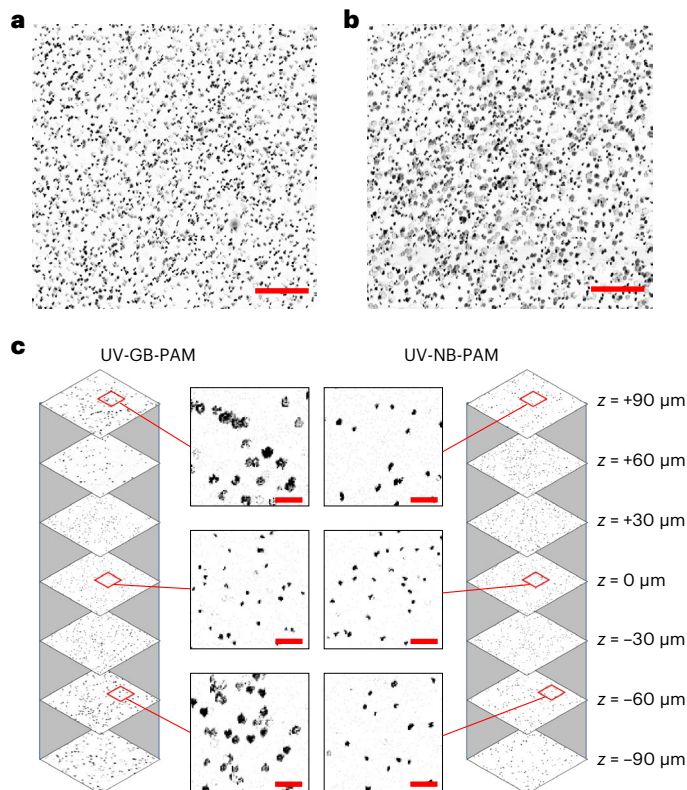


Fig. 3 | Volumetric imaging of carbon particles using UV-GB-PAM and UV-NB-PAM with a $200 \times 1.2 \mu\text{m}$ NB. a, b, x - y MAP images of carbon particles acquired using UV-NB-PAM (a) and UV-GB-PAM (b). Scale bars, $250 \mu\text{m}$. c, Virtually sectioned x - y MAP images at different depths for UV-GB-PAM (left) and UV-NB-PAM (right) after time-dependent gain compensation. Scale bars, $50 \mu\text{m}$.

diameter. NBs with variable parameters can be generated using different DOEs and laser wavelengths. The DOE for 266 nm light was designed to generate a $200 \times 1.2 \mu\text{m}$ NB (full-width-at-half-maximum (FWHM) beam length \times minimal beam diameter, respectively), whereas the DOE for 532 nm light was designed to generate a $1,000 \times 2.3 \mu\text{m}$ NB; they were formed by 64 foci and 81 foci, respectively. The phase regulators were chosen as $0.022\pi \times m$ and $0.088\pi \times m$, where m is the focus index. The foci locations of each NB were optimized for a uniform axial intensity, as listed in Supplementary Fig. 3c,d. For a Gaussian beam with a focal spot size of $2.3 \mu\text{m}$ at 532 nm, the DOF is about $70 \mu\text{m}$ (a twofold Rayleigh length), and the size of the beam spot will expand to $\sim 31 \mu\text{m}$ at a distance of $\pm 500 \mu\text{m}$. By comparison, the $1,000 \times 2.3 \mu\text{m}$ NB maintains its diameter between $\sim 2.3 \mu\text{m}$ (at the two ends) and $\sim 2.7 \mu\text{m}$ (at the middle of the beam) over the entire $1,000 \mu\text{m}$ depth range (an ~ 28 -fold Rayleigh length) with a relatively uniform axial intensity (Supplementary Fig. 4). In addition, we compared the beam profiles of the Gaussian beam (focus diameter, $1.2 \mu\text{m}$) and the DOE-based NB ($200 \times 1.2 \mu\text{m}$) at 266 nm predicted via Fourier transform, which showed that the NB can maintain the beam spot size much better along the z axis than the Gaussian beam at the same beam diameter (Fig. 1c,d). Note that the NB has the smaller beam diameter at the two ends and a slightly larger beam diameter at the middle of the beam, which is different from the focused Gaussian beam with the smallest spot size at the focal plane.

To transform conventional reflection-mode Gaussian beam OR-PAM into NB-PAM, we placed the DOE in the beam path before the objective lens (Fig. 1e). Using a customized objective lens consisting of an achromatic doublet and a correction lens, the phase-modulated beam was converted to an NB around the original focal plane of the Gaussian beam. Using DOEs, we achieved an efficiency of up to 30% input beam energy. Compared with a Bessel beam with a

sidelobe-to-main-lobe ratio of up to 20%, the NB can be optimized to have negligible sidelobes, avoiding the need for complicated image processing in NB-PAM. In contrast to optical-resolution Gaussian beam photoacoustic microscopy (GB-PAM), NB-PAM provides better 2D images of irregular surfaces or volumetric imaging of thick specimens, as shown in the simulation results (Fig. 1f,g).

NB-PAM system performance

The resolution and DOF of NB-PAM systems were measured and compared with conventional GB-PAM. A positive 1951 USAF resolution test target was imaged at wavelengths of 266 nm and 532 nm using both GB-PAM and NB-PAM. Images of the resolution target using ultraviolet GB-PAM (UV-GB-PAM) and UV-NB-PAM were acquired at different axial locations (Fig. 2a), which clearly demonstrate the improved DOF. UV-GB-PAM has an effective NA of 0.16, whereas the DOE for the $200 \times 1.2 \mu\text{m}$ NB was used for UV-NB-PAM. Note that the DOF can be slightly larger than $200 \mu\text{m}$ since we defined the NB length using the middle part. The simulation results of the beam diameter and intensity at the different axial positions were calculated for both a $1.2 \mu\text{m}$ Gaussian beam and the $200 \times 1.2 \mu\text{m}$ NB (Supplementary Fig. 5). The close-up images for both UV-GB-PAM and UV-NB-PAM (Fig. 2b and Fig. 2d, respectively) show a good image quality and a well-resolved pattern at the focal plane ($z = 0 \mu\text{m}$). By contrast, UV-GB-PAM generated a blurred image at a depth of $105 \mu\text{m}$ (Fig. 2c), whereas UV-NB-PAM still maintained the image quality (Fig. 2e). The profiles of element 6 from group 7 measured using both UV-GB-PAM and UV-NB-PAM at $z = 0 \mu\text{m}$ are shown in Fig. 2f. The lateral resolution was measured by imaging a sharp edge and quantified using edge spread functions and derived line spread functions (Fig. 2g). Conventional UV-GB-PAM has an FWHM resolution of $1.1 \mu\text{m}$ at 266 nm, which corresponds to a DOF of $\sim 30 \mu\text{m}$. The measured FWHM resolution for UV-NB-PAM is about $1.2 \mu\text{m}$, which matches well with the theoretical calculations. Similarly, we imaged the resolution target using visible GB-PAM (VIS-GB-PAM) and VIS-NB-PAM with the $1,000 \times 2.3 \mu\text{m}$ NB (Supplementary Fig. 6).

The 3D volumetric imaging capabilities of UV-NB-PAM with the $200 \times 1.2 \mu\text{m}$ NB and VIS-NB-PAM with the $1,000 \times 2.3 \mu\text{m}$ NB were compared with conventional UV-GB-PAM and VIS-GB-PAM of 0.16 NA through the imaging of carbon particles and fibres randomly distributed in a thick agarose block. The x - y maximal amplitude projection (MAP) image of particles over a depth of $\sim 400 \mu\text{m}$ acquired using UV-NB-PAM (Fig. 3a) shows more uniform particle sizes and clearer images in comparison with the MAP image acquired by UV-GB-PAM (Fig. 3b), benefitting from the improved DOF. Another piece of evidence of the improved image quality can be found from the y - z MAP images of a small fraction of carbon particle phantoms (Supplementary Fig. 7). The y - z projection image for UV-NB-PAM shows well-maintained particle sizes at different depths, whereas the UV-GB-PAM image shows noticeable blurring in out-of-focus particles due to the limited DOF. It is worth mentioning that the confocally aligned ultrasonic transducer also has a limited DOF (Supplementary Fig. 8), which affects the detection sensitivity of photoacoustic signals at different depths. To compensate for the sensitivity difference along the z axis, we implemented time-dependent gain compensation in the photoacoustic signals after differentiating the photoacoustic signals and background noise by a threshold of three times the standard deviation of the background noise. With the time-dependent gain compensation, the acoustic signal difference at different depths due to the limited acoustical DOF was alleviated. By applying virtual sectioning using time-of-flight information, we can isolate the particles at different depths with a step size of the acoustical resolution (that is, $\sim 30 \mu\text{m}$), determined via the ultrasonic transducer bandwidth. In the sectioned UV-GB-PAM images (Fig. 3c, left), it is clear that the particles distributed at a distance (that is, $z = 90 \mu\text{m}$) from the focal plane (that is, $z = 0 \mu\text{m}$) are severely blurred and distorted, whereas the UV-NB-PAM images (Fig. 3c, right) show an improved image quality.

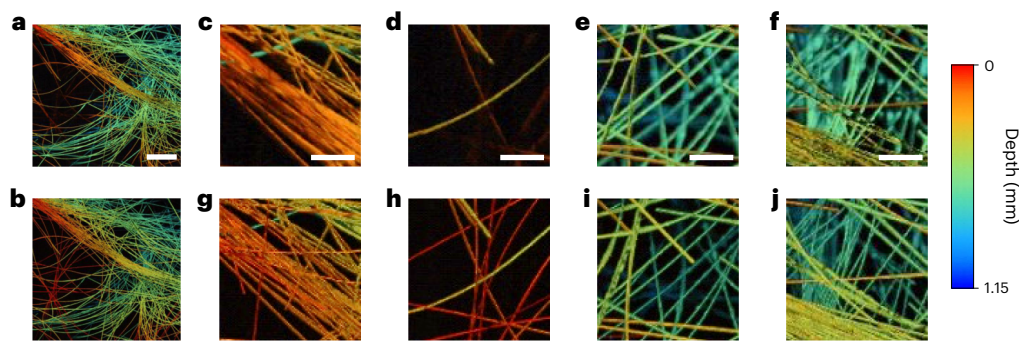


Fig. 4 | Depth-resolved imaging of carbon fibres for VIS-GB-PAM and for VIS-NB-PAM with the $1,000 \times 2.3 \mu\text{m}$ NB. **a, b**, Images of $\sim 6 \mu\text{m}$ carbon fibres randomly distributed in an agarose block, obtained using VIS-GB-PAM (**a**) and

VIS-NB-PAM (**b**). Scale bar, 1 mm. **c–j**, Comparison of close-up VIS-GB-PAM images (**c–f**) with close-up VIS-NB-PAM images (**g–j**), respectively, demonstrates the improved DOF. Scale bars, $250 \mu\text{m}$. The colour scale applies to all panels.

In addition, we acquired the depth-encoded MAP images of carbon fibres randomly distributed within an agarose phantom, using both conventional VIS-GB-PAM (Fig. 4a) and VIS-NB-PAM with the $1,000 \times 2.3 \mu\text{m}$ NB (Fig. 4b). The depth information is encoded in the different colours, ranging from 0 mm to 1.15 mm. The close-up images show that VIS-GB-PAM cannot image fibres at a distance from the focal plane in high resolution and with high sensitivity (Fig. 4c–f). By contrast, the VIS-NB-PAM images (Fig. 4g–j) show more fibres without blurring within a 1 mm depth. The optical focal plane is located at a depth of ~ 0.5 mm.

Slide-free histological imaging by UV-NB-PAM

Utilizing the strong absorption of UV light by DNA/RNA, label-free UV-GB-PAM has been demonstrated to acquire histology-like images without the need for excessive sample preparation²⁵. However, slide-free histology imaging usually faces difficulties when imaging irregular surfaces in high resolution. To demonstrate the advantages of UV-NB-PAM for fast slide-free histology imaging, we compared conventional UV-GB-PAM and UV-NB-PAM for imaging slide-free fresh organs with irregular surfaces. The UV-GB-PAM image of a mouse lung (Fig. 5a) shows blurred cell nuclei in the close-up image as well as missing features (as highlighted by the yellow arrow in Fig. 5a), which are caused by the limited DOF and the large height fluctuation in the organ surface. The small fraction of the brighter part in Fig. 5a indicates the areas around the optical focal plane of UV-GB-PAM, which has a better signal-to-noise ratio and a better resolution than the out-of-focus areas. By contrast, the UV-NB-PAM of the lung (Fig. 5b) shows some well-resolved lung features that are not identifiable in the UV-GB-PAM image (as indicated by the yellow arrow). The close-up image in Fig. 5b shows well-distinguished cell nuclei, whereas the corresponding area in the UV-GB-PAM image is blurred. In addition, we imaged unprocessed fresh mouse-brain samples in top view using both UV-GB-PAM (Fig. 5c) and UV-NB-PAM (Fig. 5d). The comparison between the close-up images acquired using conventional UV-GB-PAM (Fig. 5c) and UV-NB-PAM (Fig. 5d) clearly demonstrates the advantage of UV-NB-PAM for slide-free histological imaging, which usually requires a large DOF for unprocessed specimens that have irregular surfaces. Note that there was still some residual blood inside the major cortical blood vessels, which also generated some photoacoustic signals. This can be easily avoided via saline perfusion before brain collection. Additional images of a fresh mouse liver acquired using UV-NB-PAM and UV-GB-PAM can be found in Supplementary Fig. 9.

In vivo VIS-NB-PAM of mouse-brain vasculature

With the capability of imaging oxyhaemoglobin and deoxyhaemoglobin in a label-free manner, VIS-GB-PAM has been used widely to image both the brain vasculature and function. However, the large

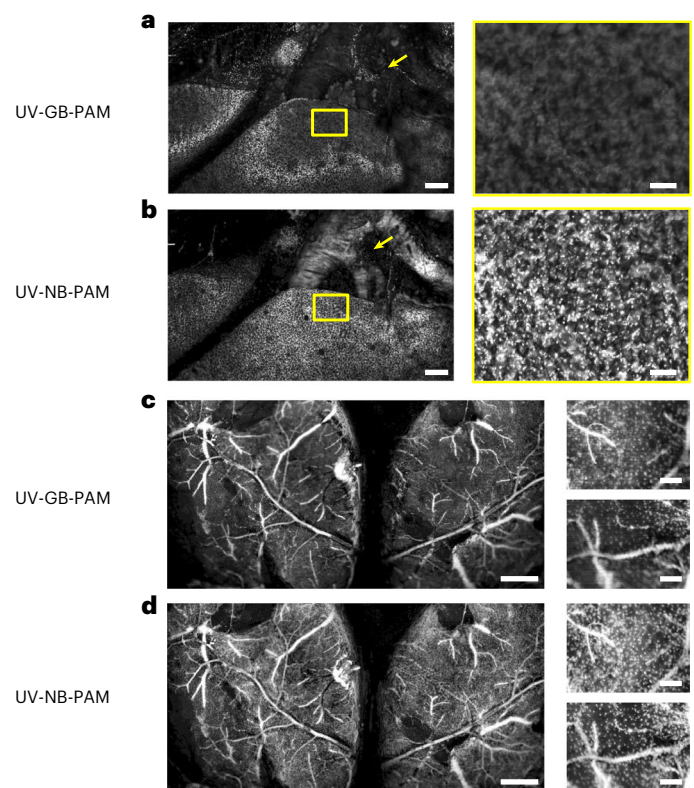


Fig. 5 | Label-free UV-GB-PAM and UV-NB-PAM with the $200 \times 1.2 \mu\text{m}$ NB for slide-free fresh mouse lung and brain samples. **a, b**, Left, images of a fresh mouse lung embedded in an agarose block obtained using UV-GB-PAM (**a**) and UV-NB-PAM (**b**). Scale bars, $250 \mu\text{m}$. Right, close-up images of the area indicated by the yellow box show the difference between UV-GB-PAM and UV-NB-PAM. Scale bars, $50 \mu\text{m}$. **c, d**, Left, images of a fresh mouse brain embedded in an agarose block using UV-GB-PAM (**c**) and UV-NB-PAM (**d**). Scale bars, $500 \mu\text{m}$. Right, close-up images of representative areas using UV-GB-PAM (**c**) show the compromised image quality due to out-of-focus locations, and close-up images using UV-NB-PAM (**d**) show the well-maintained resolution in the corresponding areas. Scale bars, $100 \mu\text{m}$.

curvature of the mouse-brain cortex affects the fast high-resolution imaging of the full cortical vessels. To demonstrate the advantages of VIS-NB-PAM for in vivo brain vasculature imaging, we imaged a mouse brain with an intact skull and a mouse brain with the skull removed via craniotomy. For better visualization of the brain curvature, we encoded the depth into different colours. Although the conventional VIS-GB-PAM of the mouse brain without a skull shows small cortical

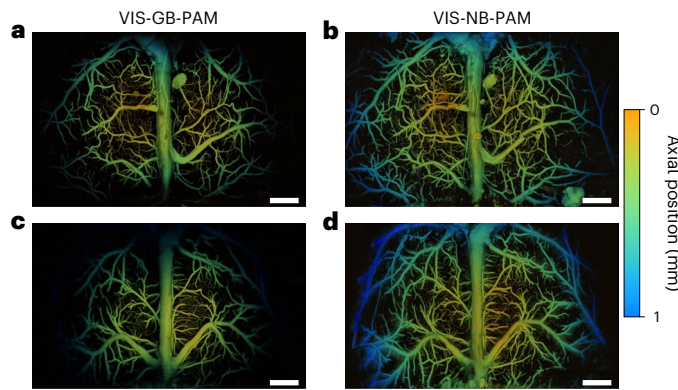


Fig. 6 | In vivo label-free depth-encoded VIS-NB-PAM with the $1,000 \times 2.3 \mu\text{m}$ NB and VIS-GB-PAM of brain vasculature with and without a skull. **a, b**, VIS-GB-PAM (**a**) and VIS-NB-PAM (**b**) of a mouse brain without a skull show the depth-encoded brain vasculature. Scale bars, 1 mm. **c, d**, VIS-GB-PAM (**c**) and VIS-NB-PAM (**d**) for a mouse with an intact skull show the depth-encoded brain vasculature. Scale bars, 1 mm. Both of the mouse-brain vasculature images obtained using VIS-NB-PAM show more blood vessels around the edge areas compared with conventional VIS-GB-PAM. The colour scale applies to all panels.

vessels in detail, it missed many vessels around the edge areas (Fig. 6a). By contrast, colour-encoded VIS-NB-PAM clearly shows more vessels around the edge areas, even at a distance of 700–800 μm away from the top surface (Fig. 6b). The irregular non-vessel-shaped structures in Fig. 6a,b may be due to imperfect surgical procedures, which resulted in minor bleeding in the brain. The VIS-GB-PAM of a mouse brain with an intact skull shows fewer blood vessels (Fig. 6c) than the mouse brain without a skull, which is mostly due to scattering by the skull and the attenuation of light. Although such skull scattering also affects the NB, the VIS-NB-PAM image still shows more vessels and a better image quality (Fig. 6d) than conventional VIS-GB-PAM. Some edge areas with vessels are slightly blurred, which may be due to the skull's impact on light propagation. It took about 20 min to scan the brain vasculature with a step size of 1.25 μm for the fast axis and 5 μm for the slow axis.

Discussion

In this work, we have designed high-efficiency DOEs to generate NBs for both VIS-NB-PAM (532 nm) and UV-NB-PAM (266 nm) in reflection mode. The NB has an elongated DOF for high-resolution imaging, which is crucial for the 2D imaging of uneven surfaces or 3D volumetric imaging. Utilizing the NB, we have demonstrated an approximately 6-fold DOF improvement in UV-NB-PAM and around a 14-fold DOF improvement in VIS-NB-PAM. Note that the current DOF improvements are not the theoretical limit, which can be further adjusted according to the laser energy and required efficiency for PAM. Using UV-NB-PAM, the slide-free histological imaging of fresh organs has been demonstrated, which shows clear advantages compared with conventional UV-GB-PAM systems. This approach addresses the critical challenge of the high-resolution imaging of uneven surfaces in unprocessed slide-free specimens and enables rapid intraoperative pathological diagnostics via photoacoustic histology. In addition, we demonstrated the in vivo VIS-NB-PAM of mouse-brain vessels with an improved field of view and DOF at the wavelength of 532 nm.

Our work brings new opportunities not only for PAM techniques but also for other high-resolution microscopic technologies for biological and biomedical applications where a large DOF is needed. Supplementary Table 3 compares our NB-PAM approach with previously developed methods for extending DOF values in PAM (a detailed discussion can be found in Supplementary Note). With minimal modifications, the DOE-based NB can convert most of the current microscopy systems for an extended DOF. The NB generated via phase-only

modulation can be combined with other structure illuminations (for example, multiple foci) and fast-scanning approaches (for example, galvo scanning) to further improve the imaging speed. It is worth noting that the imaging speed of our current PAM approach is still quite slow due to the limited motor scanning speed for VIS-PAM (that is, $<10 \text{ mm s}^{-1}$) and the relatively low laser repetition rate for UV-PAM (that is, 10 kHz). The development of fast OR-PAM with NBs will exploit the advantages of the NB in time-sensitive applications. Compared with spatial light modulators, the DOEs have a much higher damage threshold, which enables versatile applications. In addition, although we only demonstrated two wavelengths (that is, 266 nm and 532 nm) for ex vivo histological imaging and in vivo vasculature imaging via PAM, more wavelengths can easily be adopted for functional and metabolic PAM imaging. We believe that this approach will provide new opportunities for high-resolution PAM applications.

Online content

Any methods, additional references, Nature Portfolio reporting summaries, source data, extended data, supplementary information, acknowledgements, peer review information; details of author contributions and competing interests; and statements of data and code availability are available at <https://doi.org/10.1038/s41566-022-01112-w>.

References

- Glaser, A. K. et al. Light-sheet microscopy for slide-free non-destructive pathology of large clinical specimens. *Nat. Biomed. Eng.* **1**, 0084 (2017).
- Liu, S. & Hua, H. Extended depth-of-field microscopic imaging with a variable focus microscope objective. *Opt. Express* **19**, 353–362 (2011).
- Li, B., Qin, H., Yang, S. & Xing, D. In vivo fast variable focus photoacoustic microscopy using an electrically tunable lens. *Opt. Express* **22**, 20130–20137 (2014).
- Xiao, S., Tseng, H., Gritton, H., Han, X. & Mertz, J. Video-rate volumetric neuronal imaging using 3D targeted illumination. *Sci. Rep.* **8**, 7921 (2018).
- Shain, W. J., Vickers, N. A., Goldberg, B. B., Bifano, T. & Mertz, J. Extended depth-of-field microscopy with a high-speed deformable mirror. *Opt. Lett.* **42**, 995–998 (2017).
- Patel, K. B. et al. High-speed light-sheet microscopy for the in-situ acquisition of volumetric histological images of living tissue. *Nat. Biomed. Eng.* **6**, 569–583 (2022).
- Descloux, A. et al. Combined multi-plane phase retrieval and super-resolution optical fluctuation imaging for 4D cell microscopy. *Nat. Photon.* **12**, 165–172 (2018).
- Geissbuehler, S. et al. Live-cell multiplane three-dimensional super-resolution optical fluctuation imaging. *Nat. Commun.* **5**, 5830 (2014).
- Abrahamsson, S. et al. Fast multicolor 3D imaging using aberration-corrected multifocus microscopy. *Nat. Methods* **10**, 60–63 (2013).
- Oudjedi, L. et al. Astigmatic multifocus microscopy enables deep 3D super-resolved imaging. *Biomed. Opt. Express* **7**, 2163–2173 (2016).
- Zheng, G., Horstmeyer, R. & Yang, C. Wide-field, high-resolution Fourier ptychographic microscopy. *Nat. Photon.* **7**, 739–745 (2013).
- Planchon, T. A. et al. Rapid three-dimensional isotropic imaging of living cells using Bessel beam plane illumination. *Nat. Methods* **8**, 417–423 (2011).
- Gao, L., Shao, L., Chen, B.-C. & Betzig, E. 3D live fluorescence imaging of cellular dynamics using Bessel beam plane illumination microscopy. *Nat. Protoc.* **9**, 1083–1101 (2014).
- Jia, S., Vaughan, J. C. & Zhuang, X. Isotropic three-dimensional super-resolution imaging with a self-bending point spread function. *Nat. Photon.* **8**, 302–306 (2014).

15. Hu, Y., Chen, Z., Xiang, L. & Xing, D. Extended depth-of-field all-optical photoacoustic microscopy with a dual non-diffracting Bessel beam. *Opt. Lett.* **44**, 1634–1637 (2019).
16. Yang, J., Gong, L., Shen, Y. & Wang, L. V. Synthetic Bessel light needle for extended depth-of-field microscopy. *Appl. Phys. Lett.* **113**, 181104 (2018).
17. Thériault, G., Koninck, Y. D. & McCarthy, N. Extended depth of field microscopy for rapid volumetric two-photon imaging. *Opt. Express* **21**, 10095–10104 (2013).
18. Thériault, G., Cottet, M., Castonguay, A., McCarthy, N. & De Koninck, Y. Extended two-photon microscopy in live samples with Bessel beams: steadier focus, faster volume scans, and simpler stereoscopic imaging. *Front. Cell. Neurosci.* <https://doi.org/10.3389/fncel.2014.00139> (2014).
19. Snoeyink, C. Imaging performance of Bessel beam microscopy. *Opt. Lett.* **38**, 2550–2553 (2013).
20. Wu, Y. et al. Three-dimensional virtual refocusing of fluorescence microscopy images using deep learning. *Nat. Methods* **16**, 1323–1331 (2019).
21. Jin, L. et al. Deep learning extended depth-of-field microscope for fast and slide-free histology. *Proc. Natl Acad. Sci. USA* **117**, 33051–33060 (2020).
22. Zhou, Y., Sun, N. & Hu, S. Deep learning-powered Bessel-beam multi-parametric photoacoustic microscopy. *IEEE Trans. Med. Imaging* <https://doi.org/10.1109/TMI.2022.3188739> (2022).
23. Wang, L. V. & Hu, S. Photoacoustic tomography: in vivo imaging from organelles to organs. *Science* **335**, 1458–1462 (2012).
24. Wang, L. V. & Yao, J. A practical guide to photoacoustic tomography in the life sciences. *Nat. Methods* **13**, 627–638 (2016).
25. Wong, T. T. W. et al. Fast label-free multilayered histology-like imaging of human breast cancer by photoacoustic microscopy. *Sci. Adv.* **3**, e1602168 (2017).
26. Shi, J. et al. High-resolution, high-contrast mid-infrared imaging of fresh biological samples with ultraviolet-localized photoacoustic microscopy. *Nat. Photon.* **13**, 609–615 (2019).
27. Wong, T. T. W. et al. Label-free automated three-dimensional imaging of whole organs by microtomy-assisted photoacoustic microscopy. *Nat. Commun.* **8**, 1386 (2017).
28. Zhang, C., Zhang, Y. S., Yao, D.-K., Xia, Y. & Wang, L. V. Label-free photoacoustic microscopy of cytochromes. *J. Biomed. Opt.* **18**, 020504 (2013).
29. Yao, J. et al. High-speed label-free functional photoacoustic microscopy of mouse brain in action. *Nat. Methods* **12**, 407–410 (2015).
30. Cao, R. et al. Functional and oxygen-metabolic photoacoustic microscopy of the awake mouse brain. *Neuroimage* **150**, 77–87 (2017).
31. Cao, R. et al. Photoacoustic microscopy reveals the hemodynamic basis of sphingosine 1-phosphate-induced neuroprotection against ischemic stroke. *Theranostics* **8**, 6111–6120 (2018).
32. Zhou, Y., Xing, W., Maslov, K. I., Cornelius, L. A. & Wang, L. V. Handheld photoacoustic microscopy to detect melanoma depth in vivo. *Opt. Lett.* **39**, 4731–4734 (2014).
33. He, Y. et al. Label-free imaging of lipid-rich biological tissues by mid-infrared photoacoustic microscopy. *J. Biomed. Opt.* **25**, 106506 (2020).
34. Buma, T., Conley, N. C. & Choi, S. W. Multispectral photoacoustic microscopy of lipids using a pulsed supercontinuum laser. *Biomed. Opt. Express* **9**, 276–288 (2017).
35. Maslov, K., Zhang, H. F., Hu, S. & Wang, L. V. Optical-resolution photoacoustic microscopy for *in vivo* imaging of single capillaries. *Opt. Lett.* **33**, 929–931 (2008).
36. Hu, S., Maslov, K. & Wang, L. V. Second-generation optical-resolution photoacoustic microscopy with improved sensitivity and speed. *Opt. Lett.* **36**, 1134–1136 (2011).
37. Park, B. et al. Reflection-mode switchable subwavelength Bessel-beam and Gaussian-beam photoacoustic microscopy in vivo. *J. Biophotonics* **12**, e201800215 (2019).
38. Jiang, B., Yang, X. & Luo, Q. Reflection-mode Bessel-beam photoacoustic microscopy for in vivo imaging of cerebral capillaries. *Opt. Express* **24**, 20167–20176 (2016).
39. Shi, J., Wang, L., Noordam, C. & Wang, L. V. Bessel-beam Grueneisen relaxation photoacoustic microscopy with extended depth of field. *J. Biomed. Opt.* **20**, 116002 (2015).
40. Xu, Z. et al. Cortex-wide multiparametric photoacoustic microscopy based on real-time contour scanning. *Neurophotonics* **6**, 035012 (2019).
41. Ning, B. et al. Ultrasound-aided multi-parametric photoacoustic microscopy of the mouse brain. *Sci. Rep.* **5**, 18775 (2015).
42. Yang, X., Jiang, B., Song, X., Wei, J. & Luo, Q. Fast axial-scanning photoacoustic microscopy using tunable acoustic gradient lens. *Opt. Express* **25**, 7349–7357 (2017).
43. Liu, S. et al. GPU-accelerated two dimensional synthetic aperture focusing for photoacoustic microscopy. *APL Photonics* **3**, 026101 (2018).
44. Jeon, S., Park, J., Managuli, R. & Kim, C. A novel 2-D synthetic aperture focusing technique for acoustic-resolution photoacoustic microscopy. *IEEE Trans. Med. Imaging* **38**, 250–260 (2019).
45. Amjadi, M., Mostafavi, S. M., Chen, J., Wang, L. & Luo, Z. Super-resolution photoacoustic microscopy via modified phase compounding. *IEEE Trans. Med. Imaging* <https://doi.org/10.1109/TMI.2022.3184711> (2022).
46. Amjadi, M. et al. Super-resolution photoacoustic microscopy using structured-illumination. *IEEE Trans. Med. Imaging* **40**, 2197–2207 (2021).
47. Yang, J. et al. Motionless volumetric photoacoustic microscopy with spatially invariant resolution. *Nat. Commun.* **8**, 780 (2017).

Publisher's note Springer Nature remains neutral with regard to jurisdictional claims in published maps and institutional affiliations.

Springer Nature or its licensor (e.g. a society or other partner) holds exclusive rights to this article under a publishing agreement with the author(s) or other rightsholder(s); author self-archiving of the accepted manuscript version of this article is solely governed by the terms of such publishing agreement and applicable law.

© The Author(s), under exclusive licence to Springer Nature Limited 2022

Methods

Design and fabrication of the DOEs

Our fabrication is based on four rounds of lithography to achieve 16 heights, corresponding to a phase step of $\pi/8$, on a fused silica wafer. The phase modulation P is coupled with the structure height H via the relationship $P = 2\pi H(n' - 1)/\lambda$, where n' is the refractive index of silica and λ is the wavelength of the incident laser. The average height interval (HI) is 33 nm for the 266 nm laser and 72 nm for the 532 nm laser. The first round of etching is to finish $8 \times$ HI, the second is for $4 \times$ HI, the third is for $2 \times$ HI, and the fourth is for HI. The fabrication process was completed at the Stanford Nanofabrication Facility, and the detailed procedure is listed in Supplementary Table 2. The overall time cost of manufacturing one batch of DOEs is about 10 h. The height accuracy during the fabrication is better than 95%, and the alignment error for the four rounds of photolithography is around 1 μm . Our results show an axial intensity uniformity of $\sim 3.6\%$ for the $200 \times 1.2 \mu\text{m}$ NB (266 nm) and $\sim 11.1\%$ for the $1,000 \times 2.3 \mu\text{m}$ NB (532 nm). The axial intensity uniformity is calculated as below:

$$\text{Uniformity} = \frac{\text{Maximal intensity} - \text{minimal intensity}}{\text{Maximal intensity} + \text{minimal intensity}}$$

Note that the maximal intensity and minimal intensity were calculated only within the length of the NB. The DOE efficiency is calculated as the ratio of the energy enclosed within the main lobe of the NB to the energy of the input Gaussian beam. To accommodate the DOE efficiency, we used a higher input pulse energy for the NB to ensure similar signal-to-noise ratios for the Gaussian beam and the NB at the focal plane.

NB-PAM system

The ultraviolet PAM (UV-PAM) system used a Nd:YLF (neodymium-doped yttrium lithium fluoride) Q-switched 266 nm nanosecond pulsed laser (QL266-010-O, CrystaLaser), and the visible PAM (VIS-PAM) system used a 532 nm nanosecond pulsed laser (VGEN-G-20, Spectra Physics). Both the UV-PAM system and the VIS-PAM system included a pair of plano-convex lenses for beam expansion and a high-energy pinhole for spatial filtering. The expanded and collimated laser beam was focused through a customized ring-shaped ultrasonic transducer using a custom-made water-immersion objective lens. To achieve the NB for an extended DOF, we placed the customized DOE on the front surface of the objective lens. The specimen for UV-PAM was immersed in water, whereas the specimen and animal for VIS-PAM were placed underneath the water tank with a transparent membrane at the bottom. In the UV-PAM system, a bandpass glass filter (FGUV5, Thorlabs) was used to filter out the leaked pump green light. A reconfigurable I/O (input/output) device (myRIO-1900, National Instruments) was used to synchronously trigger the UV laser pulses, motor scanning and data acquisition. In the VIS-PAM system, since the 532 nm laser cannot be externally triggered, a beamsplitter and a photodiode (PDA36A, Thorlabs) were used to capture the laser pulses and synchronize the motor scanning and data acquisition. The VIS-PAM system synchronization and control were achieved using a multifunction I/O device (PCIe-6323, National Instruments). Both systems included two low-noise amplifiers (ZFL-500LN+, Mini-Circuits) and a 500 MHz sampling rate data-acquisition card (ATS 9350, Alazar Technologies).

For system characterization, we used a positive 1951 USAF resolution target (RIDSIP, Thorlabs) to confirm the image quality and the DOF. The USAF resolution target is mounted on a 3D scanner for raster scanning and adjustment of the axial position. The pulse energy was kept below 10 nJ to avoid potential damage to the USAF resolution target. The carbon fibre phantom was prepared using 3D randomly distributed carbon fibres with a diameter of $\sim 6 \mu\text{m}$ embedded in a 4% agarose block. The $2\text{--}12 \mu\text{m}$ diameter carbon particles (484164, MilliporeSigma) were chosen to prepare the agarose-embedded particle phantom.

UV-NB-PAM and UV-GB-PAM of fresh animal organs

Animal organs were collected from adult Hsd:ND4 Swiss Webster mice (male, 9–10 weeks old, Envigo) and washed using phosphate-buffered saline to remove blood on the surface. The washed fresh organs were then immersed in 2–3% low-melting-point agarose (A6013, Millipore-Sigma) at a temperature of 37 °C. The agarose with the organs was cooled using a refrigerator at 4 °C for 10 min to form strong gel blocks. The agarose-embedded organ block was then mounted onto a sample holder for PAM imaging. The images were acquired via 2D raster scanning of the sample holder immersed in the water tank.

In vivo VIS-NB-PAM and VIS-GB-PAM of mouse brains

We used C57BL/6N Hsd mice (female, 5–6 weeks old, Jackson Laboratory) for the in vivo studies. The animal was firstly anaesthetized with isoflurane ($\sim 2\text{--}3\%$ in 1.5 litre min^{-1} medical grade air) in an induction chamber via a vaporizer and then transferred to a heating pad with a nose cone for surgery. During surgery, the anaesthesia was maintained at 1.5% in 1 litre min^{-1} medical grade air. After the mouse was anaesthetized, a toe pinch procedure was conducted to confirm the anaesthesia status before any surgical procedure. When the animal no longer reacted to the toe pinch, it was transferred to a stereotactic frame with its body temperature maintained via a heating pad. Before surgery, the animal was given a single dose of 5 mg per kg (body weight) ketoprofen. Ophthalmic ointment was applied topically to the corneal surfaces before surgery to prevent corneal drying. After removing the hair on the scalp, the skin was cut from the middle, and the periosteum was removed to expose the mouse brain. The mouse imaged with the skull was kept intact without thinning. The skull was kept wet using saline and covered with ultrasound gel during the PAM imaging. The mouse imaged without a skull underwent a craniotomy to expose the cortical vessels before imaging. A portion of the skull over the region of interest was removed using a dental drill. The drilling was paused every 30 s to avoid overheating of the skull while the bone dust was continuously flushed using saline. After the craniotomy, pre-soaked surgical sponges were applied to the exposed mouse brain to prevent further bleeding before the animal was transferred to the imaging site.

For PAM imaging, the mouse was placed on a customized animal holder with a tooth bar and a nose cone to stabilize the brain. The mouse was maintained under anaesthesia using 1.0–1.5% vaporized isoflurane in 1 litre min^{-1} medical air, and the body temperature was kept at 37 °C. Ultrasound gel was applied between the water tank membrane and mouse brain to ensure ultrasound coupling. The animal holder was mounted on a customized scanner together with the water tank. During the PAM imaging, the water tank and animal were moved together by the scanner, while the PAM detection module consisting of an ultrasonic transducer and a focusing lens was immersed in water and remained still. The mouse's respiration and body temperature were monitored closely to ensure its normal physiological conditions. The animal was euthanized with carbon dioxide after PAM imaging. All animal experiments were carried out in conformity with the protocol approved by the Institutional Animal Care and Use Committee of the California Institute of Technology.

Data and image processing

To reconstruct the 2D PAM MAP images, we took the amplitude of the photoacoustic A-line signals after Hilbert transform for each pixel. For 3D PAM image reconstruction, deconvolution of the A-line signals was implemented using the spatially invariant electrical impulse response of the customized ultrasound transducer to improve the axial resolution. The 3D PAM images were reconstructed using the absolute value of the Hilbert-transformed A-line signals after the deconvolution. The axial position was determined by quantifying the maximal amplitude position in the A-line signals, assuming the speed of sound was 1,500 m s^{-1} in room-temperature water. A median filter with a window size of 2×2 pixels was applied to the depth image for smooth colours.

The colour-encoded depth-resolved image was obtained by multiplying the 2D MAP image pixel by pixel with the depth image. To alleviate signal attenuation caused by the acoustical detection sensitivity difference along the axial direction, we performed the time-dependent gain compensation after differentiating the photoacoustic signals and system noise, ensuring a uniform ultrasound detection sensitivity at different axial positions. The threshold to distinguish photoacoustic signals from noise was determined by three times the standard deviation of the noise. Thus, the time-dependent gain compensation was implemented only in photoacoustic signals to avoid amplifying the system noise.

Data availability

The data that support the findings of this study are available within the paper and its Supplementary Information. The raw data are too large to be publicly shared, yet they are available for research purposes from the corresponding authors upon reasonable request.

Code availability

The code that supports the plots and images within this paper is available from the corresponding author upon reasonable request.

Acknowledgements

L.V.W. was sponsored by the United States National Institutes of Health grants R01 EB028277, U01 NS099717 (BRAIN Initiative) and R35 CA220436 (Outstanding Investigator Award). A.d.l.Z. was supported by the National Institutes of Health grants DP5OD012179 and K23CA211793, the United States National Science Foundation (NSF 1438340) and the United States Air Force (FA9550-15-1-0007).

Author contributions

R.C. and L.V.W. designed the experiment. R.C., L.L. and Y.Z. built the PAM system. J.Z. designed and fabricated the DOEs. L.D. contributed to the mask preparation and wafer dividing. L.J. and Q.Z. manufactured the ultrasonic transducer. R.C. prepared the sample and animals and performed the imaging experiment. R.C., S.D. and Y.L. contributed to image processing. L.V.W. and A.d.l.Z. supervised the project. All authors were involved in discussions and manuscript preparation.

Competing interests

L.V.W. has a financial interest in MicroPhotoAcoustics, CalPACT and Union Photoacoustic Technologies, although they did not support this work. The remaining authors declare no competing interests.

Additional information

Supplementary information The online version contains supplementary material available at <https://doi.org/10.1038/s41566-022-01112-w>.

Correspondence and requests for materials should be addressed to Adam de la Zerda or Lihong V. Wang.

Peer review information *Nature Photonics* thanks Ruiqing Ni and the other, anonymous, reviewer(s) for their contribution to the peer review of this work.

Reprints and permissions information is available at www.nature.com/reprints.